Materials Advances

PAPER

Check for updates

Constructing effective ion channels in anion exchange membranes *via* exfoliated nanosheets towards improved conductivity for alkaline fuel cells

Prem P. Sharma,†[ab] Murli Manohar [ID] †[a] and Dukjoon Kim [ID] *[a]

A series of quaternized polysulfone (QPS)-based composite membranes containing various amounts of functionalized graphitic carbon nitride (f-g-C_3N_4) nanosheets were synthesized. The synergistic effects of the incorporated nanosheets were investigated on a variety of membrane properties for alkaline fuel cell application, such as hydroxyl ion conductivity, swelling ratio, water uptake, chemical stability, and cell performance. The well-interacting architecture of the f-g-C_3N_4 nanosheets containing multiple hydrophilic sites was the main reason for the enhanced hydroxide ion conductivity of the membrane. The QPS–CN-5 membrane showed a high hydroxide ion conductivity of 16–37 mS cm^{-1} in a temperature range from room temperature to 80 °C because of the highly interlocked ionic domains of the porous tris-triazine units in the f-g-C_3N_4 nanosheets. The single-cell test of QPS–CN-5 exhibited a maximum power density of 77 mW cm^{-2}.

1. Introduction

Due to the continuous depletion of fossil fuels and the demand for eco-friendly power, the world is extensively looking for more clean and efficient energy conversion and storage devices such as lithium-ion batteries, redox flow batteries, and fuel cells.[1–6] Fuel cell technology has recently attracted a great deal of attention as it produces electricity from an electrochemical reaction between the fuel and oxygen in an efficient way without ejecting harmful pollutants such as SOx and NOx for wide stationary and mobile applications.[7–11]

The proton exchange membrane fuel cell (PEMFC) has received considerable attention[12–15] as it generates high power density by the simple operation of a membrane–electrode assembly, in which the anionic polymer membrane serves as a separator isolating the cathodes and anodes as well as a transport medium for protons. Nafion, a typical type of perfluorinated sulfonic acid polymers, is widely used for proton exchange membranes (PEMs) as its molecular structure is quite state-of-the-art.[16–20] However, its implementation in fuel cell systems has been limited because of its substantial drawbacks such as high cost, environmental concerns associated with its synthesis, and indispensable utilization of precious metal-based catalysts.[21,22]

Alkaline exchange membrane fuel cells (AEMFCs) do not possess the shortcomings of PEMFCs and show satisfactory performance and durability along with competitive cost devoid of the utilization of platinum-based precious metals.[23–25] When an alkaline exchange membrane (AEM) is employed in the fuel cell station, high hydroxide ion (OH$^-$) conductivity should be provided along with good mechanical and chemical stability. However, its cell performance still needs improvement due to the intrinsically slow movement of OH$^-$ ions and the poor chemical stability of the alkaline exchange membrane.[26] Since the last decade, several strategies have been proposed to enhance the OH$^-$ conductivity of AEMs. Block, graft, clustered, and comb-shaped polymer structures have been devised for the synthesis of AEMs to establish high OH$^-$ conductivity with low swelling. The hydrophobic/hydrophilic micro-phase separation behavior is a prerequisite for this purpose, but it is not easily realized unless the chemical structures of AEMs are quite well designed.[27–30] Another effective approach was realized by the incorporation of the merits of inorganic materials into the polymer matrix to synthesize composite membranes.[31,32] In the synthesis of composite membranes, two-dimensional (2D) nanomaterials have gained lots of attention because of their unique properties related to their large surface area.[33–35] In comparison to 2D materials, graphitic carbon nitride (g-C_3N_4) possesses much more potential than other inorganic materials including graphene oxides and boron nitrides because of some extraordinary advantages. The hydrogen bonding between the amine/imine groups in g-C_3N_4 and the alkylated quaternary ammonium groups in the polymer backbone may provide

a *School of Chemical Engineering, Sungkyunkwan University, Suwon, Gyeonggi 440 746, Republic of Korea. E-mail: djkim@skku.edu*

b *School of Chemistry, Faculty of Basic Sciences, Shoolini University, Solan 173229, Himachal Pradesh, India*

† Both authors contributed equally to this work.

sufficient hopping sites for hydroxide ions. Moreover, the existence of repetitive lattice defects supplies diffusion pathways for hydroxide ions and the robust interfacial strength between the nanosheets and polymer molecules enhances the thermal and mechanical stability of the membrane.

Polysulfone (PS) has been widely used for the preparation of polymer electrolyte membranes as it is thermally and chemically stable and cheaper than perfluorinated ionomers. However, when it is applied for AEMs, the instability associated with the chemical degradation of quaternary ammonium groups (*i.e.*, above 60 °C and high pH) *via* Hoffman elimination limits its extensive applications. The current work represents an effective route for the synthesis of a stable PS-based AEM by the Friedel–Crafts alkylation reaction, lacking the utilization of the carcinogenic chloromethyl methyl ether (CMME). The exfoliated and functionalized graphitic carbon nitride (f-g-C_3N_4) nanosheets were dispersed in the PS matrix at various compositions. The synergistic effect of the incorporated nanosheets on a variety of important membrane properties for AEMFC applications was characterized, such as hydroxyl ion conductivity, swelling ratio, water uptake, chemical stability, and cell performance.

2. Experimental section

2.1. Materials

Polysulfone (PS, M_w = 85 000 and M_w/M_n = 2.199) was obtained from Sigma-Aldrich (St. Louis, MO). Melamine powder was purchased from Sigma Aldrich (Spruse Street, St. Louis, MO, USA). Paraformaldehyde (HCHO)n, stannic chloride anhydrous ($SnCl_4$), and trimethylsilyl chloride (TMSCl) were purchased from TCI (Japan). Chloroform ($CHCl_3$), 2-propanol ($CH_3CHOHCH_3$), methanol (CH_3OH), deionized (DI) water, *N*-methyl-2-pyrrolidone (NMP), trimethylamine (TMA), and dichloromethane were obtained from Daejung Chemicals (Korea). Nafion solution (5 wt%, EW 1100) was purchased from Du Pont (Delaware, USA), while platinum (nominally 40% on carbon black, HiSPEC 4000) was purchased from Alfa Aesar (Ward Hill, MA).

2.2. Synthesis of g-C_3N_4 and f-g-C_3N_4

Bulk g-C_3N_4 was synthesized by a thermal oxidation etching process. Briefly, 5 g of white melamine powder was placed in an alumina crucible and subjected to a muffle furnace at 550 °C for 4 h at a heating and cooling rate of 5 °C min^{-1}. The obtained yellow powder was milled into a finer powder with the help of a mortar. The functionalization and exfoliation of bulk g-C_3N_4 were carried out by an acid oxidation process. 1 g of fine powder was dispersed in a 10 M sulfuric acid (H_2SO_4) solution. After complete dispersion, 5 g $K_2Cr_2O_7$ was slowly added under continuous stirring for 48 h at room temperature. The product was neutralized with DI water and then centrifuged at 6000 rpm for 10 min at least three times. The final product was collected and freeze-dried to obtain the functionalized and exfoliated nanosheets, f-g-C_3N_4.

2.3. Chloromethylation and quaternization of PS

The chloromethylation of PS was achieved at 45 °C following a previous report.[36] Briefly, 10 g PS was slowly dissolved in chloroform to avoid lump formation. Chloromethylation was achieved by the addition of $SnCl_4$ (0.7 mL) and HCHO (13.5 g) to trimethylsilyl chloride (57 mL). The whole mixture was stirred for 72 h at 45 °C. The color of the solution slowly changed from milky white to pink, indicating the Friedel–Crafts alkylation reaction. The final product (white solid) was obtained by precipitating the mixture in 2-propanol. To convert the chloromethyl group into the quaternized ammonium group, the chloromethylated PS (CMPS) product was dissolved in a mixture of NMP and chloroform (80 : 20 v/v) followed by the addition of trimethylamine (30%). The resulting mixture was stirred at 65 °C for 12 h and then cast on a clean glass plate for a pre-calculated thickness of ~80 μm. The final product was termed as quaternized PS (QPS).

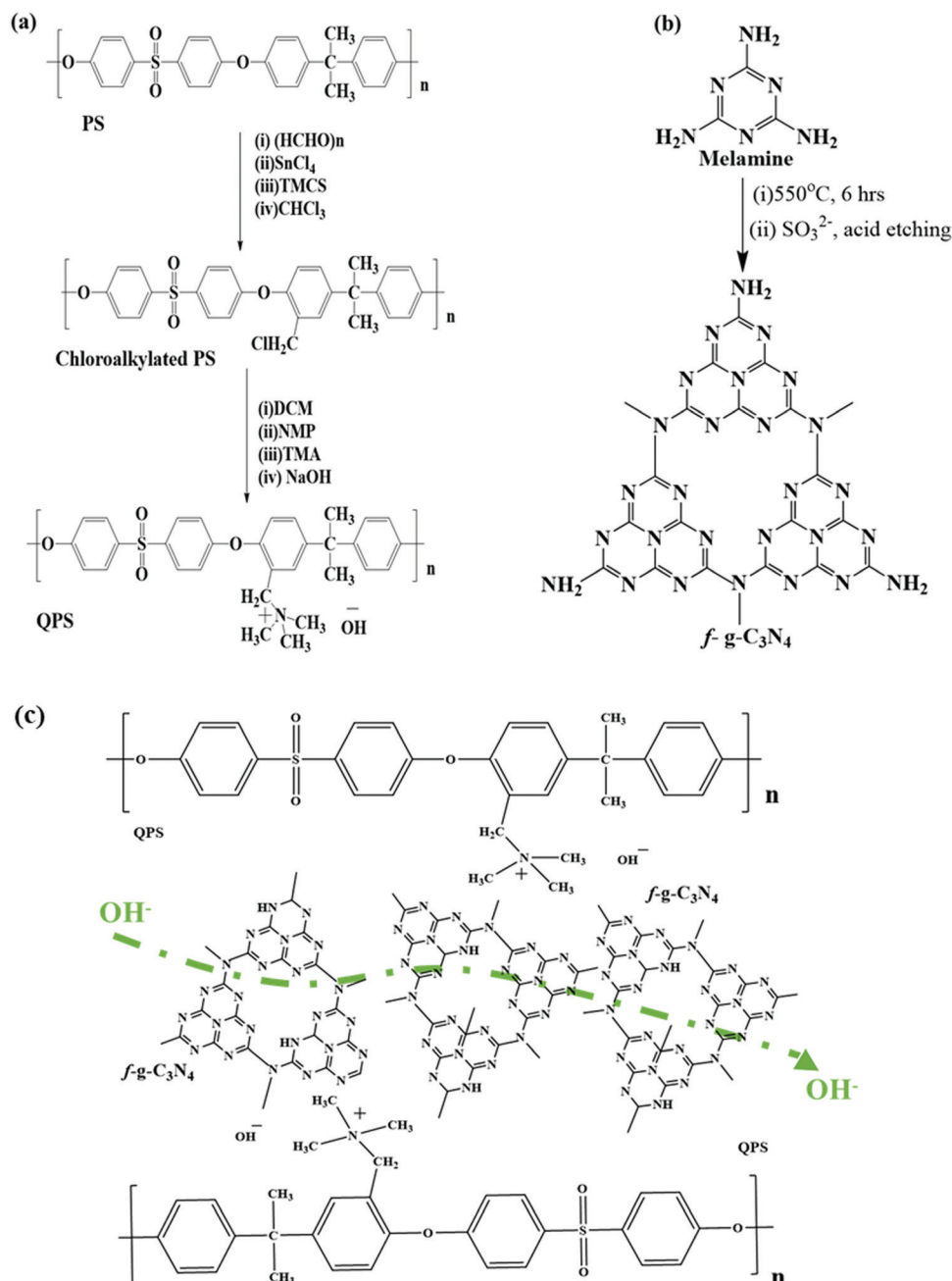### 2.4. Preparation of QPS–CN*x* composite membranes

The composite membrane, QPS–CN*x* (where *x* denotes the wt% of f-g-C_3N_4), was synthesized by a simple blending method. QPS and f-g-C_3N_4 nanosheets were dispersed into a mixture of NMP and chloroform (80 : 20 v/v) and then subjected to quaternization with trimethylamine as discussed earlier. After this, the homogeneous mixture was cast on a clean Petri dish and then dried for 12 h at 70 °C under vacuum. The dry membrane was separately dipped into a 1 M hydroxide (NaOH) solution for complete alkalization. Scheme 1 illustrates the synthetic routes of QPS, f-g-C_3N_4, and QPS–CN*x*.

2.5. Characterization

2.5.1. Chemical structure analysis. Fourier-transform infrared (FT-IR) spectra were recorded using a PerkinElmer FT-IR spectrometer (Nicolet iS10, Brucker IFS 66/S, Brucker, Germany) in a wavenumber range of 4000–400 cm^{-1}. The chloroalkylation of PS was characterized by ^{1}H nuclear magnetic resonance spectrometry (^{1}H NMR, Varian Unity INOVA 500 MHz, Varian, Paoli Alto, California, USA) using CDCl$_3$ as a solvent. The shape and size of the g-C_3N_4 nanosheets and the morphology of the composite membranes were evaluated by field emission scanning electron microscopy (FE-SEM, EM, Phillip XL30 ESEM-FCG, North Billerica, Ma). The crystalline structures of both the nanosheets and the polymer were determined by X-ray diffraction spectroscopy (D8 Advance, Bruker, Billerica, MA, USA) with CuKα radiation (λ = 1.54 Å). The stepwise weight loss of the nanosheets and composite membranes was characterized by thermogravimetric analysis (TGA, Seiko Exstar 6000, Japan). Energy-dispersive X-ray spectroscopy and high-resolution transmission electron microscopy (EDS/HR-TEM, JEM-ARF 200F, Japan) were employed for elemental mapping and obtaining high-resolution micro-images of the composite membranes.

2.5.2. Ion exchange capacity (IEC). The IEC of the membranes was determined three times by Mohr's titration method. The membrane samples were washed with DI water and

Scheme 1 Synthetic schemes of (a) QPS, (b) f-g-C_3N_4, and (c) QPS−CNx.

completely dried to measure their weight before immersion in 0.1 M NaCl solution. The membrane samples charged with Cl^- ions were further immersed in a 0.5 M Na_2SO_4 solution for complete exchange of the Cl^- ions with SO_4^{2-} ions. The released chloride ions were titrated against 0.1 M $AgNO_3$ using potassium chromate as an indicator. The IEC (meq g^{-1}) values of the membranes were calculated using eqn (1):

$$\text{IEC} = \frac{C_{Cl} \times V_{sol}}{W_{dry}} \tag{1}$$

where C_{cl} is the concentration of Cl^- in the extracted solution,

V_{sol} is the volume of titrated or consumed $AgNO_3$ and W_{dry} is the dry membrane weight.

2.5.3. Anion conductivity. The membranes were immersed in water and then cut into 3 cm (length) × 1 cm (width) sections with a thickness of $\sim 80 \pm 5$ μm to measure the hydroxide ion conductivity. The sample was placed in a 4-probe cell (BEKK-TECH, USA) and the in-plane anion conductivity was measured by alternating current (AC) impedance spectroscopy (Zahner IM6e, Germany) in the frequency range of 1 Hz to 1 MHz at 5 mV under 100% relative humidity. The bulk resistance of the membrane was directly obtained from the impedance curve and the hydroxide ion conductivity was determined from the

resistance using eqn (2):

$$\sigma = \frac{L}{RWT} \qquad (2)$$

Here, σ is the anion conductivity of the membrane in mS cm^{-1}, L is the distance in the direction of ion flow between the measurement probes in cm, R is the bulk resistance of the membrane in Ohm, W is the width of the membrane in cm, and T is the thickness of the membrane in cm.

Another important parameter in the polymer electrolyte is the activation energy, and low activation energy is favorable for the easy transportation of ions. It is obtained from the temperature-dependent hydroxide ion conductivity. The activation energy (E_a) was determined using the following equation:

$$\sigma = \mathrm{In}\sigma^\circ - \frac{E_a}{RT} \qquad (3)$$

where σ° represents the pre-exponential factor, R represents the gas constant, and T is the temperature in K (Kelvin).

2.5.4. Water uptake and swelling ratio. Water uptake is important for ion exchange membranes because it estimates the hydrophilicity of the membrane. There are two types of water present inside the membrane, which are mainly in the form of bound water and free water. The transportation of ions takes place mostly through the bound water by the hopping mechanism. As the g-C$_3$N$_4$ nanosheet has polar groups at its periphery, it helps the membrane to absorb water. The quaternary ammonium group in the polymer also tends to form hydrogen bonds with the water molecule, and thus aids the hopping of OH$^-$ ions.

Water uptake was calculated using the following equation:

$$\mathrm{WU}(\%) = \frac{\mathrm{Wet_w} - \mathrm{Dry_w}}{\mathrm{Dry_w}} \qquad (4)$$

where $\mathrm{Wet_w}$ and $\mathrm{Dry_w}$ are the weights of the wet and dry membranes, respectively. Water uptake was measured three times for each membrane.

The swelling ratio of the membrane was calculated using eqn (5):

$$\text{Swelling ratio} = \frac{L_s - L_d}{L_d} \qquad (5)$$

where L_s and L_d are the lengths of the wet and dry samples, respectively.

The hydration number was also calculated using the following equation, where λ is the number of water molecules attached per quaternary ammonium functional group, WU is the water uptake and IEC is the ion exchange capacity (meq g^{-1}). Eqn (6) is used for the calculation of the hydration number:

$$\lambda = \frac{10 \times \mathrm{WU}}{\mathrm{IEC} \times 18.02} \qquad (6)$$

2.5.5. Thermal and chemical stability. A thermogravimetric analyzer (TGA, Seiko Exstar 6000, Japan) was used to investigate the thermal stability of the bulk and functionalized forms of the g-C$_3$N$_4$ nanosheets and QPS–CNx composite

membranes. The sample was thermally scanned at a ramping rate of 10 °C min^{-1} from 30 °C to 800 °C in a nitrogen gas atmosphere.

The QPS–CNx samples with dimensions of 3 cm × 1 cm were immersed in a 3 M NaOH solution for 300 h at room temperature. Each sample was taken out of the solution to be washed with water repeatedly to check the chemical and physical changes in the membranes. After regular intervals of time, the IEC value was measured by the method mentioned earlier. The IEC values of the QPS and QPS–CNx membranes were collected to justify their chemical stability.

2.5.6. Oxidative stability. The anti-oxidation of QPS and QPS–CNx was investigated by measuring the residual weight percentage of each membrane after Fenton's test. The completely dry membranes were immersed in Fenton's solution (3 wt% H$_2$O$_2$, 4 ppm Fe^{2+}) at 80 °C for 24 h. After the samples were taken out of the solution, they were washed several times with DI water and then dried at 80 °C. The residual weight (RW) % was calculated from the difference between the weight of the samples before (m_b) and after treatment (m_a) using eqn (7).

$$RW(\%) = \frac{m_a}{m_b} \times 100 \qquad (7)$$

2.5.7. Membrane electrode assembly and fuel cell performance. The catalyst ink was prepared by mixing 0.1 g Pt/C (40%), 0.66 g Nafion ionomer (5 wt% in IPA), 1 mL DI water, and 8.042 g isopropanol. The mixture was sonicated using a horn-type sonicator (Sonomasher, SL Science, Korea) for 30 min for good dispersion. The mixture was sprayed onto a carbon paper for 5–10 min using a hand spray pistol to prepare a gas diffusion layer (GDL). The membrane electrode assembly (MEA) was prepared by pressing the catalyst-coated membrane using a heating press (Ocean Science, Korea) at 110 °C and 5 MPa for 3 min. The active area of the MEA for this process was 6.25 cm^2 and the Pt loading amounts for both the anode and the cathode were 0.5 mg cm^{-2} each. The fuel cell performance was measured using a unit cell station (SPPSN-300) provided by CNL Energy (Korea). During the cell test, hydrogen and oxygen gas was continuously fed to the anode and cathode sites at a flow rate of 300 cm^3 min^{-1} each. The fuel cell performance was measured at 80 °C under 100% relative humidity (RH).

3. Results and discussion

3.1. Chemical and physical structure of the g-C$_3$N$_4$ nanosheets

The crystalline and chemical structure of the bulk and exfoliated forms of the g-C$_3$N$_4$ nanosheets were investigated by XRD and XPS. Fig. 1(a) shows a comparison of the XRD spectra of the bulk and functionalized g-C$_3$N$_4$ nanosheets. A peak observed at 13.1° is due to the inter-planar structural packing of the bulk g-C$_3$N$_4$ nanosheets.[37] Another strong peak (002) observed at 27.4° from bulk g-C$_3$N$_4$ originates from the interlayer reflection and crystal stacking of the nanosheets,[38] which is due to the delocalization of π-electrons in the aromatic

ring by the alternating carbon and nitrogen atoms of g-C$_3$N$_4$. After acid exfoliation, this peak is remarkably reduced and slightly shifted to 27.8°, confirming the loss of ordered crystalline structures of the stacked sheets.[39–41]

The chemical compositions of the bulk and exfoliated forms of the g-C$_3$N$_4$ nanosheets were investigated by XPS, as shown in Fig. 1(b). The peaks at 288 eV and 400 eV correspond to the binding energies of C 1s and N 1s, respectively. The peak intensity at 528 eV stemming from the oxygen in f-g-C$_3$N$_4$ is much stronger than that in bulk g-C$_3$N$_4$, because of the generation of –C=O and –COOH groups during the oxidation (functionalization) process with concentrated H$_2$SO$_4$. The dominant peaks arising at 396 and 398 eV (Fig. 1(c)) are attributed to the sp^2 hybridized nitrogen atoms in the tris- and triazine rings and tertiary carbons, as shown in Scheme 1(b) and (c). A prominent peak appears at 284.3 eV, attributed to the coordination of the surface adventitious carbon present in the triazine ring at an alternate position with the nitrogen atom, whereas another peak at 284.8 eV is attributed mainly to the carbon bonded with oxygen atoms over the surface of graphitic carbon nitride (Fig. 1(d)). All the above-mentioned elemental analyses through XPS confirm the presence of the elements C, N and O over the surface of graphitic carbon nitride.

The morphological difference between the bulk g-C$_3$N$_4$ nanosheets and f-g-C$_3$N$_4$ nanosheets inside the QPS matrix was investigated through SEM and TEM images, as shown in Fig. 2. As shown in the SEM image in Fig. 2(a), the bulk g-C$_3$N$_4$ nanosheet structure is characterized by micron or few submicron sizes of aggregates in the stacked form. These stacked

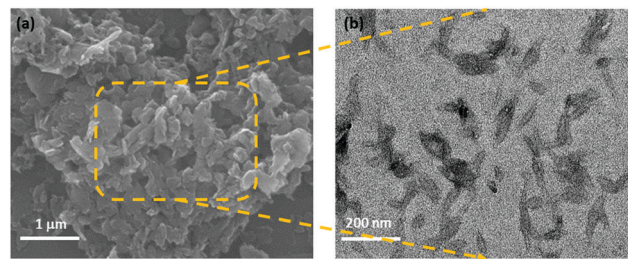Fig. 2 (a) SEM image of bulk g-C$_3$N$_4$ and (b) TEM image of exfoliated f-g-C$_3$N$_4$.

aggregates of nanosheets are not dispersed well inside the QPS matrix and thus become a barrier for the tortuous conduction of ions. When those are treated with a strong oxidizing agent, it causes destabilization in the van der Waals forces between the stacked sheets and thus the f-g-C$_3$N$_4$ nanosheets are quite well dispersed after acid exfoliation, as confirmed by the TEM image in Fig. 2(b). Being exfoliated, the flux of hydroxide ions through the nano-channels provided by the polar functional groups will be enhanced, resulting in the enhancement of ionic conductivity and cell performance.

3.2. Chemical and physical structure of the composite membranes

The chloromethylation and quaternization of PS was confirmed by ^{1}H NMR and FT-IR spectroscopy. As shown in Fig. 3(a), the ^{1}H NMR spectrum of pristine PS was characterized by 6.9–7.9 (multi-H atoms in the phenyl group at 6.9–7.9 ppm and the
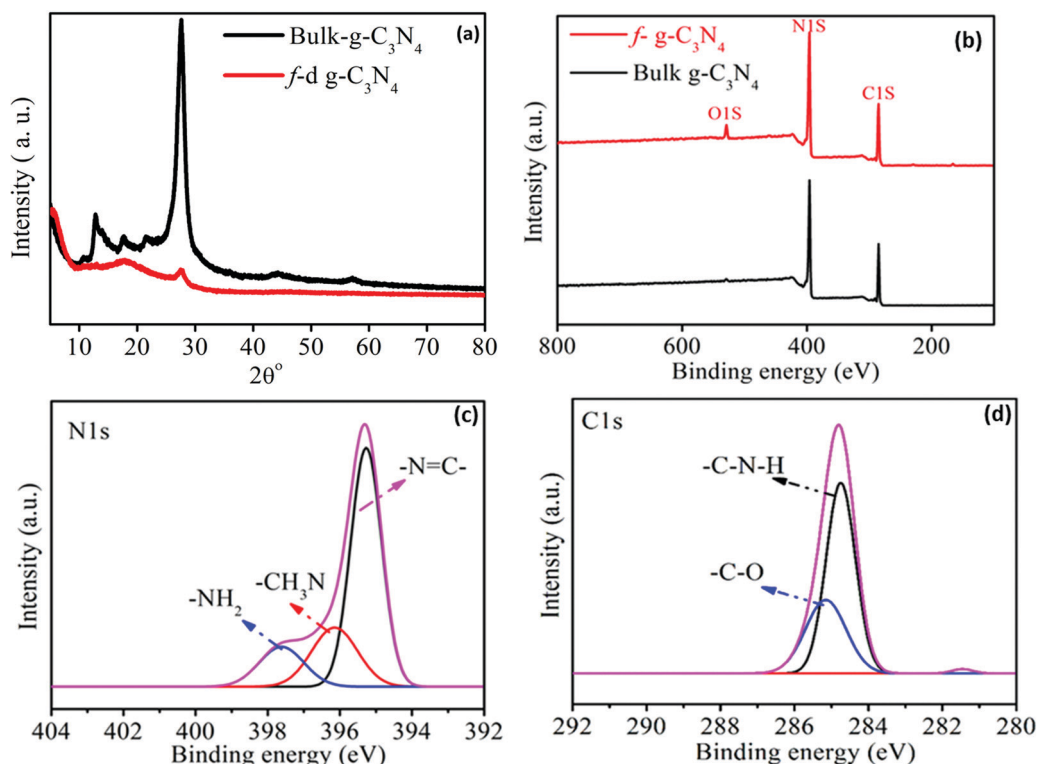

Fig. 1 (a) XRD spectra and (b) XPS spectra of the bulk and functionalized g-C$_3$N$_4$. (c) N 1s and (d) C 1s XPS spectra of g-C$_3$N$_4$.
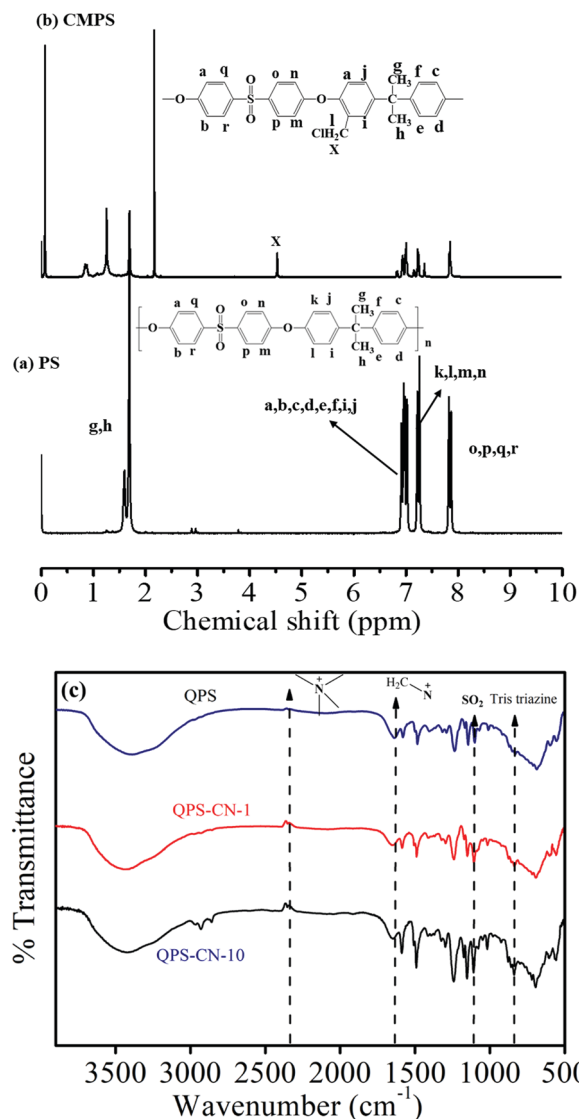
Fig. 3 (a, b) ^{1}H NMR of PS (polysulfone) and CMPS (chloromethylated polysulfone). (c) FT-IR spectra of QPS, QPS–CN-1 and QPS–CN-10.

Fig. 4 (a) SEM images of the QPS and QPS–CN-5 membranes and (b) cross-sectional elemental mapping images of the QPS–CN-5 membrane.

methyl group at 1.7 ppm). Chloromethylation occurred at the activated aryl ring between the isopropyl and ether bonds, and thus the presence of the CH_2Cl peak is assured by the occurrence of a single proton signal at 4.6 ppm, which was originally absent in pristine PS. As this signal intensity increased with reaction time (72 h), the degree of chloromethylation (DCM) was estimated using eqn (8):[42]

$$DCM = \frac{2A(Hd)}{A(Hc)} \qquad (8)$$

Here, $A(Hd)$ is the integral area of the signal for the proton attached at the l position of the phenyl ring in CMPS, while $A(Hc)$ is that for pristine PS. In this study, the degree of chloromethylation was ∼44.01%, which enables the subsequent quaternization process. The quaternization of CMPS was confirmed by ATR-FTIR analysis of QPS and its composite membranes, as shown in Fig. 3(b). The IR bands at 1240 and
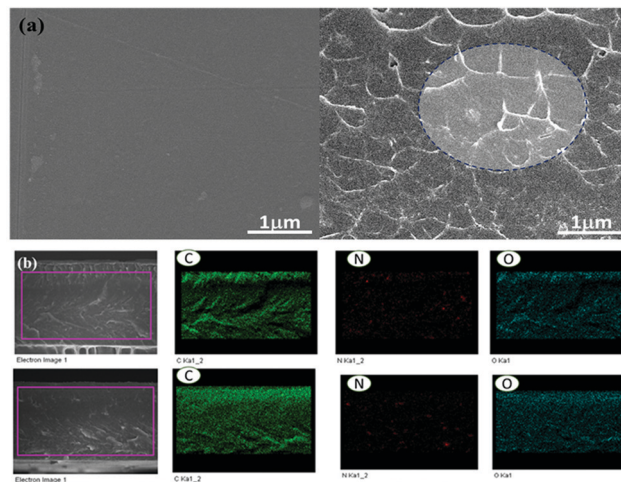
1146 cm^{-1} occur due to the presence of the sulfone group (O=S=O) in QPS. The characteristic IR bands at 1672 cm^{-1} and 2340–2375 cm^{-1} confirm the presence of quaternary ammonium groups in the PS backbone. One more characteristic band occurring at 805 cm^{-1} confirms the presence of the tris-triazine unit in graphitic carbon nitride.

The dispersive morphology of the synthesized nanosheets in the polymer electrolyte membrane was analyzed by FE-SEM. As shown in Fig. 4(a), the surface image of the pristine QPS membrane shows a dense and homogeneous morphology without any defect. The cross-sectional image of the QPS–CN-5 membrane, however, clearly shows the presence of f-g-C_3N_4 nanosheets well dispersed in the PS matrix. The interfaces between these two phases were quite stable due to the affiliated ionic interaction between the electronegative elements of f-g-C_3N_4 and the quaternary ammonium groups of PS. The elemental compositions were investigated by EDS to confirm their dispersion state (Fig. 4(b)). There was no sign of agglomeration of the nanosheets in the QPS–CN-5 membrane, as all elemental mappings indicate the good compatible and dispersive nature of f-g-C_3N_4 in the QPS matrix.

3.3. Thermal, optical, and flexible properties

The thermal stability of the bulk and functionalized g-C_3N_4 nanosheets and QPS–CNx composite membranes was characterized by thermogravimetric analysis (TGA). No evidence of degradation was observed up to 600 °C in the bulk g-C_3N_4 nanosheets, whereas a minute weight loss occurred in the f-g-C_3N_4 ones due to the presence of adsorbed water. These TGA results reveal the hydrophilic nature of the f-g-C_3N_4 nanosheets due to the existence of numerous hydroxyl groups. Additionally, the ultimate degradation of g-C_3N_4 occurs beyond 550 °C, as confirmed by the dTg curve (inset) in Fig. 5(a), revealing the stability of the nanosheets for fuel cell performance application at elevated temperatures. Three-step weight loss was observed for the QPS–CNx composite membranes at 150, 300, and 450 °C due to the absorbed water, degradation of
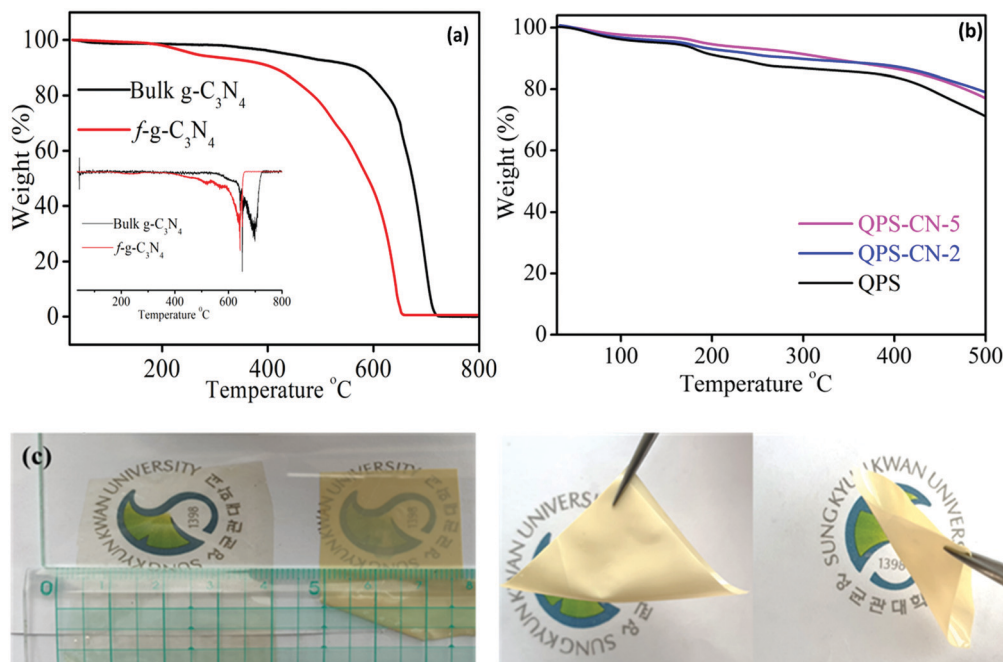
Fig. 5 TGA behavior of the (a) bulk and functionalized $g\text{-}C_3N_4$ (dTg spectra inserted) and (b) QPS and QPS–CNx membranes. (c) Optical images of the QPS and QPS–CN-5 membranes.

functional groups, and polymer backbone degradation, respectively. As shown in Fig. 5(b), the decomposition of QPS–CN-2 and QPS–CN-5 begins at a lower temperature than that of pristine QPS for this reason. The optical images of the pristine and composite membranes were quite different from each other, as shown in Fig. 5(c). While the QPS membranes were transparent, the QPS–CN-5 membrane was translucent due to the presence of nanosheets with different refractive indices from the QPS matrix. Moreover, both the pristine and composite membranes illustrate quite flexible and bendable properties.

3.4. Anion conductivity

The anion conductivity of the QPS–CNx composite membranes is shown in Fig. 6(a). There is an increment in the ionic conductivity with increasing temperature when the f-g-C_3N_4 nanosheet content is fixed. Ion conductivity also increased with increasing f-g-C_3N_4 nanosheet content up to 5 wt%, but then decreased when its content was raised to 10 wt%. The increment in ionic conductivity is directly related to the water uptake because water molecules are the medium for hydroxide ion transport. As expected, the QPS–CN-5 membrane exhibited the highest ionic conductivity of 22 mS cm^{-1} at 40 °C, while that of the pristine QPS membrane was 16 mS cm^{-1}. The temperature dependence of the anion conductivity of commercial FAPQ-375-PP has also been added for reference.[43] Ion conductivity increases with temperature because of the enhanced thermal motion of the hydroxide ions at elevated temperatures. Moreover, as the temperature is elevated, the increased free volume of the membrane accommodated more water, and thus the ion conductivity increases. The presence of smooth ionic channels affects

the activation energy (E_a) for ion conduction. As discussed above, the ionic interaction between the nanofiller and polymer backbone provides an easier pathway for ionic conduction. This feasible ion conduction can reduce the activation energy, which can be calculated by the Arrhenius plot of the temperature dependence of conductivity. As shown in Fig. 6(b), the activation energy is 10.30 KJ mol^{-1} for QPS–CN-5 and 13.08 KJ mol^{-1} for QPS–CN-10. As demonstrated in Fig. 6(c), the presence of hydroxyl and amino groups can hold more water molecules by hydrogen bonding, which in turn contributes to promoting hydroxyl ion transport, while the quaternary ammonium groups in the polymer matrix provide hopping sites for hydroxyl ion transport, and the inner pores of exfoliated sheets construct the diffusion pathways for hydroxyl ions. It acts as a medium to facilitate fast ion conduction, but it is diminished when its content is beyond a certain level as it leads to the blockage of the diffusion pathway due to agglomeration. Consequently, an adequate amount of the functionalized and exfoliated forms of these nanosheets improves the ionic conductivity and dimensional stability of the membrane.

3.5. Water uptake and swelling ratio

The swelling ratio and water uptake are vital properties for a membrane in fuel cell applications. These properties are directly related to the number of quaternary ammonium groups of QPS in this case. When the membrane absorbs more water molecules, the diffusion sites via the formation of hydrogen bonding networks also increase. Although high water uptake leads to high ionic conductivity, the excessive water inclusion deteriorates the mechanical property of the membrane. Fig. 7(a) presents the temperature dependence of water uptake. As expected, increment in water uptake was observed for all the
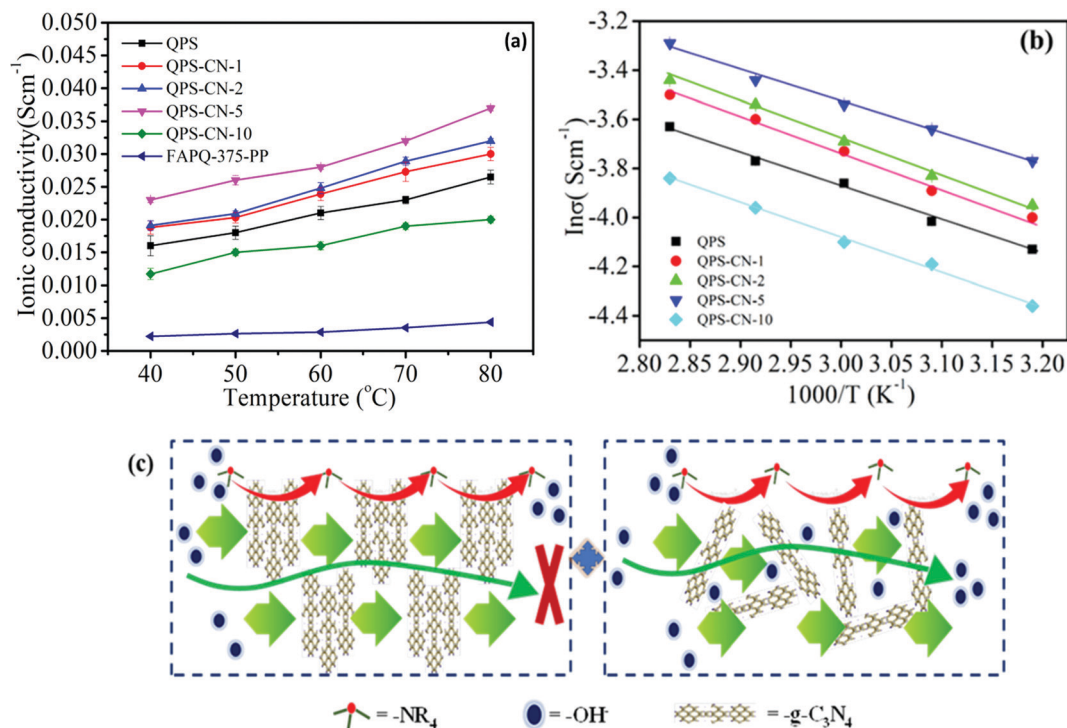
Fig. 6 (a) Temperature dependence of ionic conductivity and (b) its Arrhenius behavior for the QPS and QPS–CNx composite membranes. (c) The proposed mechanism for improved ionic conductivity.

membranes at temperatures from 40 to 80 °C because of the free volume increment. The water uptake of the composite membrane increases with increasing nanosheet content up to 5 wt% because the presence of lots of voids and the high surface area of the two-dimensional nanosheets lead to an increase in the hydrophilicity of the composite membrane, as mentioned above. However, the water uptake of QPS–CN-10 (containing 10 wt% nanosheets) becomes lower than that of pristine QPS because the very strong ionic interaction of the nanofillers with QPS molecules restricts the polymer chain mobility, which prevents water absorption and thus controls the swelling degree as well. As we can see from Fig. 7(b), the swelling degree for the membranes is maximum for QPS–CN-5 at 30 °C for the same reasons as that of the water uptake. The same trend can be observed in the case of the hydration number as it is represented as the number of water molecules associated per quaternary ammonium group, as shown in Fig. 7(c). The hydration number for the membranes increases with temperature because of the fast diffusion of water molecules. The enhancement in the hydrophilic and polar groups present on the surface of graphitic carbon nitride as we increase the content concentration affords more trapping sites for water molecules in the form of bound water, thus leading to a regular increment in the hydration number up to 21 for QPS–CN-5 at 80 °C.

3.6. Alkaline and oxidative stabilities

Another important aspect in membrane evaluation is its stability over a long period in an alkaline environment. For this, the membrane samples were dipped in a 3 M alkaline solution for

300 h at room temperature, and their ionic conductivity was measured to analyze the chemical stability effect, as shown in Fig. 8(a). The attack of the nucleophile OH$^-$ is responsible for the degradation of quaternary ammonium groups attached on the polymer backbone (Hoffman β-elimination). In this work, Hoffman β-elimination is defeated by the following strategies. Chloromethylation is conducted by choosing the Friedel–Crafts reaction in which chloroalkyl groups are attached to the polymer backbone except for β-hydrogen atoms, and the addition of f-g-C$_3$N$_4$ improves the chemical resistance of QPS molecules by forming ionic interactions between them.

Oxidative stability is also a critical long-term stability evaluation factor. The radicals ($^\bullet$OH and $^\bullet$OOH) formed during fuel cell operation intensively attack the functional groups of the polymer backbone and thus diminish the performance of the membrane. The weight change of the membrane after Fenton's test is shown in Table 1, in which the composite membrane shows better oxidative stability than the pristine one. The functional groups and polymer backbones are counterattacked by $^\bullet$OH and $^\bullet$OOH several times. Herein, the resonance structure of the tris-triazine ring of g-C$_3$N$_4$ engages the lone pairs of nitrogen and thus results in the least chances of formation of coordination bond complexes with the Fe metal ion in Fenton's reagent, as shown in Fig. 8(b). Thus, the skeleton of the nanofiller provides a shielding effect to both the polymer backbone and functional groups from degradation at a fast rate.

In addition, to justify the incorporation of f-g-C$_3$N$_4$, Table 2 shows a comparison with other reports with respect to hydroxide ion conductivity and ion exchange capacity.[44–51]
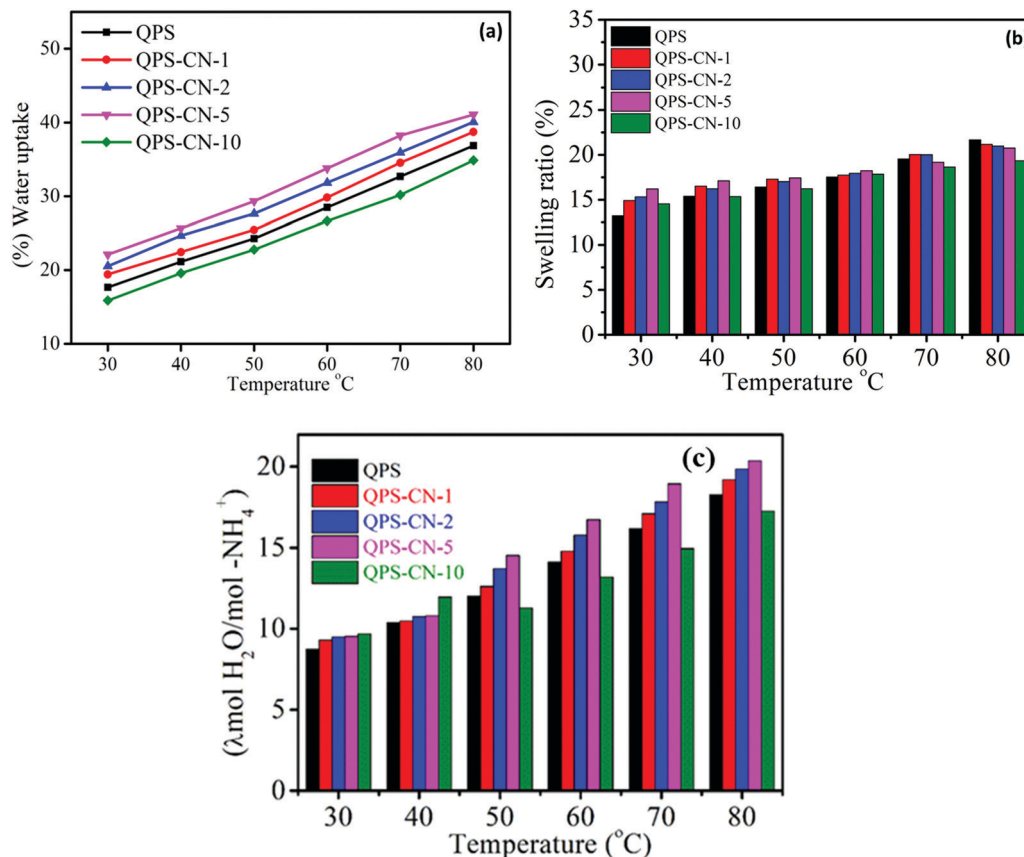
Fig. 7 (a) Water uptake, (b) swelling ratio, and (c) hydration number of the QPS and QPS–CNx composite membranes at different temperatures.

3.7. Fuel cell performance

The single-cell (H_2/O_2) performance of the pristine and composite membranes was evaluated by polarization and power density curves, as shown in Fig. 9. The catalyst-coated membranes were prepared from QPS (IEC = 1.12 meq g^{-1}) and QPS–CN-5 (IEC = 1.32 meq g^{-1}) for comparison. The fuel cell system was operated at 80 °C under 100% relative humidity conditions for both H_2 and O_2. The obtained open-circuit voltage (OCV) for QPS–CN-5 was 0.960 V, whereas it was 0.846 V for QPS. However, power densities of up to 52 mW m^{-2} for the pristine membrane and 72 mW m^{-2} for the QPS–CN-5 membrane were achieved because of the higher hydroxyl ion conductivity of QPS–CN-5. Additionally, the power densities of QPS–CN-2 and QPS–CN-10 were 49 and 41 mW cm^{-2}, respectively. This enhancement in performance suggests that the composite membrane
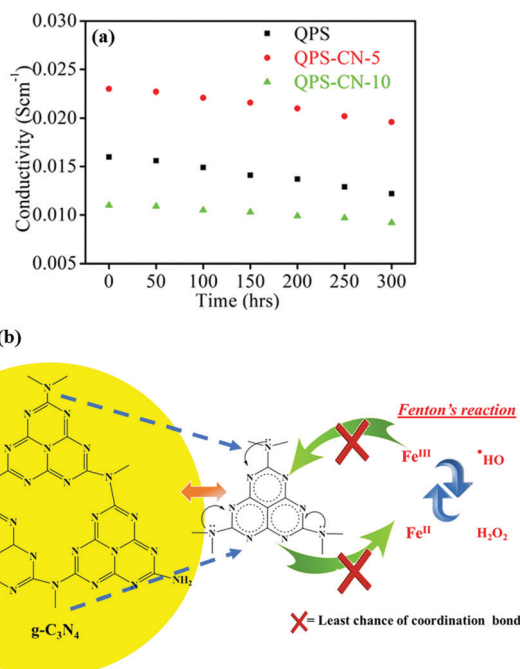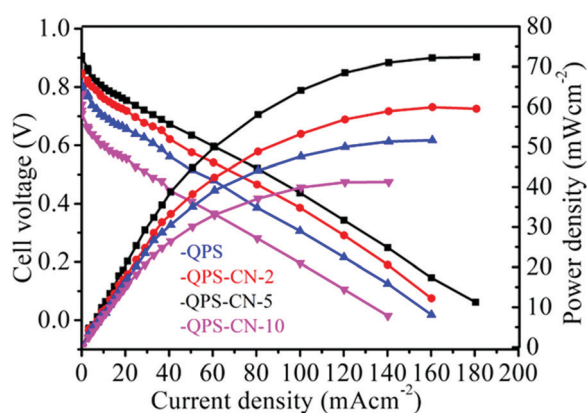

Fig. 8 (a) Alkaline stability of the QPS and QPS–CNx composite membranes in 3 M NaOH for 300 h and (b) the related mechanism showing the stability against Fenton's reagent.

Table 1 Oxidative stability of the QPS and QPS–CNx composite membranes

Membrane	Residual weight W_R (%)	Time (hours)
QPS	84.17 ± 0.6	24
QPS–CN-1	86.22 ± 0.7	24
QPS–CN-2	87.89 ± 0.5	24
QPS–CN-5	89.27 ± 0.8	24
QPS–CN-10	91.73 ± 0.5	24

Table 2 Comparison of the ionic conductivity and ion exchange capacity from recent reports[44–51]

Membrane	IEC (meq g^{-1})	Conductivity (mS cm^{-1}, 80 °C)	Ref.
QPSU-0.5%-QGs	1.20	18.73	44
c-AMPSU-0.1%-rGO	1.79	∼60	45
p-AMPSU-0.1%-rGO	1.85	∼45	45
QPSU-2%-QPbGs	1.87	49.7	46
QPSU-0.5%-QPbGs	1.83	46.3	46
Quaternized (PS) + SiO_2	1.72	20.4	47
Quaternized (PS) + ZrO_2	0.92	15.1	48
Quaternized (PAES) + ZrO_2	1.74	41.4	49
QPAES/TiO_2-1.5	1.48	35.7 ± 0.2	50
QPAES/g-C_3N_4-0.25	1.55	43.1 ± 0.2	40
QPAES/g-C_3N_4-0.6	1.60	46.5 ± 1.2	51
QPAES/g-C_3N_4-2.0	1.65	37.9 ± 0.2	51
QPS-CN-5	1.32	37	This work

Fig. 9 Cell performance of the QPS and QPS–CN*x* composite membranes at a 300 cm^3 min^{-1} H_2/O_2 flow rate under 100% RH.

synthesized in this study can be an alternative anion exchange membrane for fuel cell applications.

4. Conclusion

The optimum ionic interaction between the 2D forms of f-g-C_3N_4 nanosheets and QPS improves the swelling ratio and hydroxyl ion conductivity by ionic channel formation in a composite membrane. The successful synthesis of f-g-C_3N_4 nanosheets was proven by XRD, XPS, and FT-IR analyses, while its morphology was characterized by SEM and TEM. AEM was synthesized by chloromethylation with a degree of chloromethylation of ∼44% without CMME, proven by ^{1}H NMR. The affinity of the QPS matrix with the f-g-C_3N_4 nanosheets along with their respective elemental compositions were confirmed by their cross-sectional SEM images and EDS analysis, respectively. The QPS–CN-5 composite membrane displayed excellent chemical stability of up to 300 h in an alkaline medium and an enhanced hydroxide ion conductivity of 37 mS cm^{-1} at 80 °C. Furthermore, the OCV test demonstrated that the dropdown of voltage is mitigated for QPS–CN-5 as compared with that of pristine QPS, owing to the well-suited

interaction between the f-g-C_3N_4 nanosheets and QPS molecules, indicating its potential as an anion exchange membrane for fuel cell applications.

Conflicts of interest

The authors declare that they have no known competing financial interests or personal relationships that could have appeared to influence the work reported in this paper.

Acknowledgements

Notes and references

1 W. Wu, Y. Li, P. Chen, J. Liu, J. Wang and H. Zhang, Constructing ionic liquid-filled proton transfer channels within nanocomposite membrane by using functionalized graphene oxide, *ACS Appl. Mater. Interfaces*, 2016, **8**, 588–599.

2 F. Xu, Y. Su and B. Lin, Progress of Alkaline Anion Exchange Membranes for Fuel Cells: The Effects of Micro-Phase Separation, *Front. Mater.*, 2020, **7**, 1–7.

3 A. Muthumeenal, M. Sri Abirami Saraswathi, D. Rana and A. Nagendran, Recent research trends in polymer nanocomposite proton exchange membranes for electrochemical energy conversion and storage devices, in *Membrane Technology: Sustainable Solutions in Water, Health, Energy and Environmental Sectors*, ed. Sridhar, S., Taylor & Francis/CRC Press, Boca Raton, FL, 2018, vol. 17, pp. 351–374.

4 Y. H. Zhu, Y. B. Yin, X. Yang, T. Sun, S. Wang, Y. S. Jiang, J. M. Yan and X. B. Zhang, Transformation of Rusty Stainless-Steel Meshes into Stable, Low-Cost, and Binder-Free Cathodes for High-Performance Potassium-Ion Batteries, *Angew. Chem., Int. Ed.*, 2017, **56**, 7881–7885.

5 Y. Zhu, L. Ding, X. Liang, M. A. Shehzad, L. Wang, X. Ge and T. Xu, Beneficial use of rotatable-spacer side-chains in alkaline anion exchange membranes for fuel cells, *Energy Environ. Sci.*, 2018, **11**, 3472–3479.

6 H. G. Wang, S. Yuan, D. L. Ma, X. B. Zhang and J. M. Yan, Electrospun materials for lithium and sodium rechargeable batteries: from structure evolution to electrochemical performance, *Energy Environ. Sci.*, 2015, **8**, 1660–1681.

7 U. Lucia, Overview on Fuel Cell, *Renewable Sustainable Energy Rev.*, 2014, **30**, 164–169.

8 J. P. Lemmon, Energy: Reimagine fuel cells, *Nature*, 2015, **525**, 447–449.

9 D. Larcher and J. M. Tarascon, Towards Greener and More Sustainable Batteries for Electrical Energy Storage, *Nat. Chem.*, 2015, **7**, 19–29.

10 L. Zhu, T. J. Zimudzi, Y. Wang, X. Yu, J. Pan, D. I. Han, L. Kushner, L. Zhuang and M. A. Hickner, Mechanically

Robust Anion Exchange Membranes via Long Hydrophilic Crosslinkers, *Macromolecules*, 2017, **50**, 2329–2337.

11 L. Zhu, X. Yu, X. Peng, J. Z. Tawanda, N. Saikia, T. K. Michael and S. Song, Poly(olefin)-Based anion exchange membranes prepared using Ziegler–Natta polymerization, *Macromolecules*, 2019, **52**, 4030–4041.

12 Y.-C. Cao, X. Wang and K. Scott, The Synthesis and Characteristic of an Anion Conductive Polymer Membrane for Alkaline Anion Exchange Fuel Cells, *J. Power Sources*, 2012, **201**, 226–230.

13 Z. X. Liu, Y. Yang, W. Z. Lu, C. Wang, M. Chen and Z. Q. Mao, Durability Test of PEMFC with Pt-PFSA Composite Membrane, *Int. J. Hydrogen Energy*, 2012, **37**, 956–960.

14 M. Manohar and D. J. Kim, Advantageous of Hybrid Fuel Cell Operation under Self-Humidification for Energy Efficient Bipolar Membrane, *ACS Sustainable Chem. Eng.*, 2019, **7**, 16493–16500.

15 H. A. Gasteiger, S. S. Kocha, B. Sompalli and F. T. Wagner, Activity benchmarks and requirements for Pt, Pt-alloy, and non-Pt oxygen reduction catalysts for PEMFCs, *Appl. Catal., B*, 2005, **56**, 9–35.

16 Y. J. Wang, J. Qiao, R. Baker and J. Zhang, Alkaline polymer electrolyte membranes for fuel cell applications, *Chem. Soc. Rev.*, 2013, **42**, 5768–5787.

17 C. Lee, H. Park, H. B. Lee and Y. M. Lee, Importance of Proton Conductivity Measurement in Polymer Electrolyte Membrane for Fuel Cell Application, *Ind. Eng. Chem. Res.*, 2005, **44**, 7617–7626.

18 K.-D. Kreuer, Proton conductivity: Materials and Applications, *Chem. Mater.*, 1996, **8**, 610–641.

19 J. Pan, L. Zhu, J. Han and M. A. Hickner, Mechanically Tough and Chemically Stable Anion Exchange Membranes from Rigid-Flexible Semi-Interpenetrating Networks, *Chem. Mater.*, 2015, **27**, 6689–6698.

20 M. Manohar, P. P. Sharma and D. Kim, Intercalated poly(2-acrylamido-2-methyl-1-propanesulfonic acid) into sulfonated poly(1,4-phenylene ether-ether-sulfone) based proton exchange membrane: Improved ionic conductivity, *Molecules*, 2020, **26**(1), 161.

21 J. S. Olsson, T. H. Pham and P. Jannasch, Poly(arylene piperidinium) hydroxide ion exchange membranes: synthesis, alkaline stability, and conductivity, *Adv. Funct. Mater.*, 2018, **28**, 1702758.

22 T. H. Pham, J. S. Olsson and P. Jannasch, Effects of alicyclic anion and backbone structure on the performance of poly(terphenyl)-based hydroxide exchange membranes, *J. Mater. Chem. A*, 2019, **7**, 15895–15906.

23 Y.-J. Wang, J. Qiao, R. Baker and J. Zhang, Alkaline polymer electrolyte membranes for fuel cell applications, *Chem. Soc. Rev.*, 2013, **42**, 5768–5787.

24 M. D. Carmo, L. Fritz, J. Mergel and D. Stolten, A comprehensive review on PEM water electrolysis, *Int. J. Hydrogen Energy*, 2013, **38**, 4901–4934.

25 R. T. Slade, J. Kizewski, S. Poynton, R. Zeng and J. Varcoe, Alkaline Membrane Fuel Cells, *Fuel Cells*, 2013, 9–29.

26 A. M.-A. Mahmoud and K. Miyatake, Optimization of the pendant chain length in partially fluorinated aromatic anion exchange membranes for alkaline fuel cells, *J. Mater. Chem. A*, 2018, **6**, 14400–14409.

27 B. C. Lin, F. Xu, Y. Su, Z. J. Zhu, Y. R. Ren and J. N. Ding, Facile preparation of anion exchange membrane based on polystyrene-b-polybutadiene-b-polystyrene for the application of alkaline fuel cells, *Ind. Eng. Chem. Res.*, 2019, **58**, 22299–22305.

28 M. Tanaka, K. Fukasawa, E. Nishino, S. Yamaguchi, K. Yamada and H. Tanaka, Anion conductive block poly (arylene ether) s: synthesis, properties, and application in alkaline fuel cells, *J. Am. Chem. Soc.*, 2011, **133**, 10646–10654.

29 J. R. Varcoe, R. C.-T. Slade, E. L.-H. Yee, S. D. Poynton, D. J. Driscoll and D. C. Apperley, Poly(ethylene-co-tetrafluoroethylene) derived radiation-grafted anion-exchange membrane with properties specifically tailored for application in metal-cation-free alkaline polymer electrolyte fuel cells, *Chem. Mater.*, 2007, **19**, 2686–2693.

30 N. Li, Y. Leng, M. A. Hickner and C.-Y. Wang, Highly stable anion conductive comb shaped copolymers for alkaline fuel cells, *J. Am. Chem. Soc.*, 2013, **135**, 10124–10133.

31 B. P. Tripathi and V. K. Shahi, Organic–inorganic nanocomposite polymer electrolyte membranes for fuel cell applications, *Prog. Polym. Sci.*, 2011, **36**, 945–979.

32 K. S. Kumar, S. Rajendran and M. R. Prabhu, A Study of influence on sulfonated TiO2-Poly (Vinylidene fluoride-co-hexafluoropropylene) nano composite membranes for PEM Fuel cell application, *Appl. Surf. Sci.*, 2017, **418**, 64–71.

33 S. Gahlot, P. P. Sharma, V. Kulshrestha and P. K. Jha, SGO/SPES-based highly conducting polymer electrolyte membranes for fuel cell application, *ACS Appl. Mater. Interfaces*, 2014, **6**, 5595–5601.

34 Q. Yang, C. X. Lin, F. H. Liu, L. Li, Q. G. Zhang, A. M. Zhu and Q. L. Liu, Poly(2,6-dimethyl-1,4-phenylene oxide)/ionic liquid functionalized graphene oxide anion exchange membranes for fuel cells, *J. Membr. Sci.*, 2018, **552**, 367–376.

35 L. Yao, X. Pan, N. Li, Z. Hu and S. Chen, Improved performance of quaternized poly (arylene ether ketone) s/graphitic carbon nitride nano-sheets composite anion exchange membrane for fuel cell applications, *Appl. Surf. Sci.*, 2020, **503**, 144071.

36 M. Manohar, A. K. Das and V. K. Shahi, Efficient Bipolar Membrane with Functionalized Graphene Oxide Interfacial Layer for Water Splitting and Converting Salt into Acid/Base by Electrodialysis, *Ind. Eng. Chem. Res.*, 2018, **57**, 1129–1136.

37 J. Tian, Q. Liu, C. Ge, Z. A. Xing, M. A. Asiri, O. Al-Youbi and X. Sun, Ultrathin graphitic carbon nitride nano-sheets: a low-cost, green, and highly efficient electrocatalyst toward the reduction of hydrogen peroxide and its glucose biosensing application, *Nanoscale*, 2013, **5**, 8921–8924.

38 X. Wang, K. Maeda, A. Thomas, K. Takanabe, G. Xin, J. M. Carlsson, K. Domen and M. Antonietti, A metal-free polymeric photocatalyst for hydrogen production from water under visible light, *Nat. Mater.*, 2009, **8**, 76–80.

39 J. Xu, H.-T. Wu, X. Wang, B. Xue, Y.-X. Li and Y. Cao, A new and environmentally benign precursor for the synthesis of

mesoporous g-C3N4 with tunable surface area, *Phys. Chem. Chem. Phys.*, 2013, **15**, 4510–4517.

40 S. Z. Butler, S. M.-L. Hollen, Y. Cao, J. Cui, A. Gupta, H. R. Gutiérrez, T. F. Heinz, S. S. Hong, J. Huang and A. F. Ismach, Progress, challenges, and opportunities in two-dimensional materials beyond graphene, *ACS Nano*, 2013, **7**, 2898–2926.

41 B. V. Lotsch, M. J. Döblinger, L. Sehnert, J. Seyfarth, O. Senker and W. Oeckler, Unmasking Melon by a Complementary Approach Employing Electron Diffraction, Solid-State NMR Spectroscopy, and Theoretical Calculations—Structural Characterization of a Carbon Nitride Polymer, *Chem. – Eur. J.*, 2007, **13**, 4969–4980.

42 M. Manohar, A. K. Thakur, R. P. Pandey and V. K. Shahi, Efficient and stable anion exchange membrane: Tuned membrane permeability and charge density for molecular/ionic separation, *J. Membr. Sci.*, 2015, **15**, 250–258.

43 M. Manohar and D. Kim, Enhancement of alkaline conductivity and chemical stability of quaternized poly(2,6-dimethyl-1,4-phenylene oxide) alkaline electrolyte membrane by mild temperature benzyl bromination, *RSC Adv.*, 2020, **10**, 36704–36712.

44 L. Liu, C. Tong, Y. He, Y. Zhao and C. Lü, Enhanced properties of quaternized graphenes reinforced polysulfone based composite anion exchange membranes for alkaline fuel cell, *J. Membr. Sci.*, 2015, **487**, 99–108.

45 B. Hu, L. Miao, Y. Zhao and C. Lü, Azide-assisted cross-linked quaternized polysulfone with reduced graphene oxide for highly stable anion exchange membranes, *J. Membr. Sci.*, 2017, **530**, 84–94.

46 L. Liu, B. Hu, Y. Zhao and C. Lü, A facile construction of quaternized polymer brush-grafted graphene modified polysulfone based composite anion exchange membranes with enhanced performance, *RSC Adv.*, 2016, **6**, 51057–51067.

47 L. Liu, C. Tong, Y. He, Y. Zhao, B. Hu and C. Lü, Novel quaternized mesoporous silica nanoparticle modified polysulfone-based composite anion exchange membranes for alkaline fuel cells, *RSC Adv.*, 2015, **5**, 43381–43390.

48 R. Vinodh, M. Purushothaman and D. Sangeetha, Novel quaternized polysulfone/ZrO2 composite membranes for solid alkaline fuel cell applications, *Int. J. Hydrogen Energy*, 2011, **36**, 7291–7302.

49 X. Li, Y. Yu and Y. Meng, Novel quaternized poly(arylene ether sulfone)/nano-ZrO$_2$ composite anion exchange membranes for alkaline fuel cells, *ACS Appl. Mater. Interfaces*, 2013, **5**, 1414–1422.

50 P. B. Ingabire, X. Pan, A. Haragirimana, N. Li, Z. Hu and S. Chen, Improved hydroxide conductivity and performance of nanocomposite membrane derived on quaternized polymers incorporated by titanium dioxide modified graphitic carbon nitride for fuel cells, *Renewable Energy*, 2020, **152**, 590–600.

51 P. B. Ingabire, X. Pan, A. Haragirimana, N. Li, Z. Hu and S. Chen, Enhanced conduction capability of nanocomposite membrane of quaternized poly(arylene ether sulfone)s covalently bonded with graphitic carbon nitride nanosheets for fuel cells, *React. Funct. Polym.*, 2019, **144**, 104260.